Microfluidic Reactor Imaging

DOI: 10.1002/anie.201202967

Characterization of Microfluidic Gas Reactors Using Remote-Detection MRI and Parahydrogen-Induced Polarization**

Vladimir V. Zhivonitko, Ville-Veikko Telkki, and Igor V. Koptyug*

Nuclear magnetic resonance (NMR) is an extremely powerful method for in situ monitoring of chemical reactions and mass transport processes.[1] However, the low intrinsic sensitivity of NMR resulting from low thermal nuclear spin polarization limits the use of the method. Several hyperpolarization techniques have been developed for boosting the sensitivity.[2] Among them, parahydrogen-induced polarization (PHIP) has a direct relation to chemistry, as the hyperpolarization is naturally produced in the course of a chemical reaction proceeding through the addition of parahydrogen.[3] Originally, PHIP was discovered in a homogeneous catalytic hydrogenation, and since then many homogeneous catalytic systems have been shown to produce PHIP.[3a,c] Within the past five years, several catalysts have been found to enable the production of PHIP in heterogeneously catalyzed hydrogenations.[4,5] Catalyst–product separation is much easier in the heterogeneous than in the homogeneous processes, and therefore, continuous production of hyperpolarized molecules is facilitated.

Herein, we consider a miniaturized packed-bed reactor, which produces a continuous flow of gaseous catalyst-free hyperpolarized molecules, as a microfluidic nuclear spin polarizer based on PHIP achieved in a heterogeneous hydrogenation reaction. Microfluidics deals with the control and manipulation of fluids in channels with dimensions below one millimeter.[6] Microfluidic devices provide control over a process with capabilities that exceed those of large-scale systems.[7,8] In the production of hyperpolarized molecules utilizing PHIP, the advantages of using microfluidic flow reactors instead of large reactors are low-scale production, fast transport times through the device, highly controllable heat exchange, and much safer pressurization of the reactor. Furthermore, microfluidic flow reactors can be easily mounted inside the magnet of an NMR spectrometer, whereas large-scale polarizers have to be placed outside the magnet, leading to significant losses of polarization during the transport of the molecules to the magnet. Microfluidic reactor could be even included in a lab-on-a-chip device in which it would produce hyperpolarized substances for NMR characterization of the processes in the following modules of the device.

As the performance of the reactor is characterized by NMR, the size of a radio-frequency (RF) coil in a conventional NMR experiment is dictated by the size of an entire microfluidic device (the reactor in this case). Typically, the dimensions of the device are orders of magnitude larger than the dimensions of the flow channels inside it. In general, a small coil is more sensitive than a large coil.[9] Therefore, the poor sensitivity resulting from the large coil and a low filling factor make conventional NMR experiments very challenging, especially when gases with a low spin density are studied.

Remote-detection (RD) NMR based on the spatial separation of signal encoding and detection provides an elegant solution to the sensitivity issues.[10] In the RD MRI experiments carried out herein, the encoding of spatial information is performed by a large coil that surrounds the microfluidic reactor, while signal detection is done by an ultrasensitive microcoil with an optimized filling factor outside the device as the fluid flows out (Figure 1 a). Consequently, the RD method increases significantly the sensitivity of the experiment when compared to a conventional NMR experiment. The travel time from the encoding region to the detector depends on the spatial position of fluid molecules during the encoding, and thus RD NMR provides time-of-flight (TOF) information. Consequently, TOF flow images measured by RD MRI reveal mass transport characteristics of the device under investigation.

In our previous study, we showed that the sensitivity enhancement of several orders of magnitude can be achieved by combining PHIP and RD NMR, allowing gas flow visualization in microfluidic devices.[11] PHIP was produced by a relatively large polarizer outside the magnet. Herein, we demonstrate that miniaturized microfluidic gas reactors can provide significant polarization enhancement compared to thermal polarization of nuclear spins inside the NMR magnet, and the high polarization degree combined with RD MRI technique enable characterization of the reactors. Recently, Bouchard et al.[12] visualized hydrogenation in a larger reactor utilizing PHIP and conventional MRI. However, the sensitivity boost given by RD technique used in our work enables the investigation of much smaller reactors, and the method

[*] Dr. V. V. Zhivonitko, Prof. I. V. Koptyug
Laboratory of Magnetic Resonance Microimaging
International Tomography Center SB RAS
3A Institutskaya St., Novosibirsk 630090 (Russia)
E-mail: v_zhivonitko@tomo.nsc.ru
Dr. V.-V. Telkki
Department of Physics, NMR Research Group, University of Oulu
P.O. Box 3000, 90014 Oulu (Finland)

[**] This work was supported by the Russian Government (grant 11.G34.31.0045), RFBR (11-03-93995-CSIC_a, 11-03-00248-a, 12-03-00403-a), the program of support of leading scientific schools (NSh-7643.2010.3), and the Academy of Finland (123847 and 139839). We thank Dr. J. Lounila for fruitful discussions. I.V.K. thanks Prof. C. Bianchini and Dr. P. Barbaro (ICCOM-CNR, Sesto Fiorentino, Firenze, Italy) for providing the sample of catalyst [Rh(cod)(sulfos)]/SiO_2. V.V.Z. thanks I. E. Beck for providing the sample of catalyst Rh/TiO_2.

Supporting information for this article is available on the WWW under http://dx.doi.org/10.1002/anie.201202967.

© 2012 Wiley-VCH Verlag GmbH & Co. KGaA, Weinheim

provides more detailed insight into the transport processes influencing the hyperpolarization formation in heterogeneous hydrogenations.

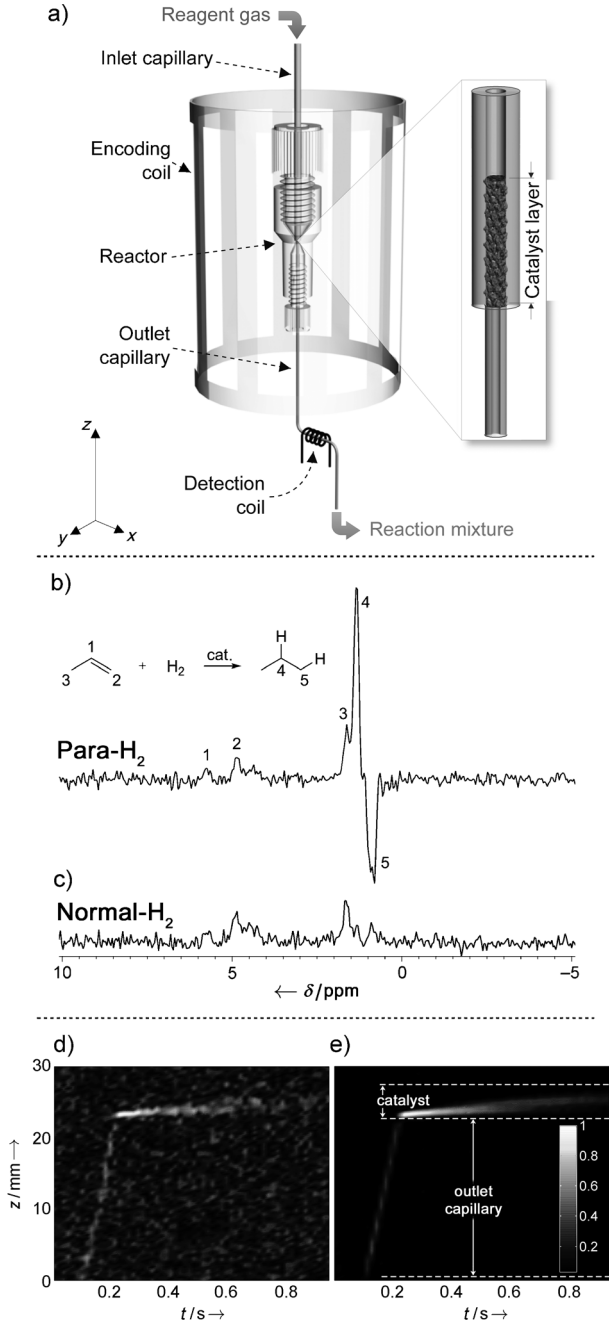

Figure 1. a) Experimental setup. Gaseous mixture containing parahydrogen and propene flows through the catalyst bed packed inside the inlet capillary close to the connection between the inlet and the outlet capillaries. Three types of capillaries of different diameters (ID 800, 405, and 150 μm) were used as the inlet capillary. The diameter of the outlet capillary was constant in all experiments (ID 150 μm). The catalyst bed was placed inside the encoding coil. b), c) ^{1}H NMR spectra of the reaction mixture measured by the detection microcoil in the experiments with b) parahydrogen and c) normal hydrogen at 22 °C. The reaction was carried out in R-800-5 reactor. d), e) *z*-Encoded RD TOF images acquired for the R-800-5 reactor at 22 °C. Normal hydrogen and parahydrogen were used for acquiring the images (d) and (e), respectively. The catalyst bed and the outlet capillary regions are shown with white dashed lines in image (e).

Three different continuous flow microfluidic reactors packed with Rh/SiO_2 catalyst were used in the experiments (Figure 1a; see also the Supporting Information). The diameters of the packed beds were 800, 405, and 150 μm, whereas their lengths were 5, 14, and 15 mm, respectively. Hereafter, the reactors are denoted as R-800-5, R-405-14, and R-150-15, respectively. Heterogeneous propene hydrogenation was employed as a model reaction process.

First, we showed that the sensitivity of the detection microcoil is high enough to acquire a good-quality ^{1}H NMR spectrum from gaseous propane produced in the R-800-5 reactor even at room temperature. As shown in Figure 1b, two strong PHIP signals with opposite phases were observed after the acquisition of only 8 scans. The absorptive signal with a larger chemical shift (4) is attributed to the hyperpolarized (HP) proton in the CH_2 group of propane, whereas the emissive signal (5) originates from a HP proton in the CH_3 group. The spectrum includes also three other signals arising from thermally polarized protons of residual propene. A similar experiment performed using normal hydrogen (hydrogen with a ca. 3:1 ortho/para spin-isomer ratio) instead of parahydrogen (hydrogen with a ca. 1:1 ortho/para spin-isomer ratio) produced the spectrum shown in Figure 1c. The reaction yield was estimated either from the decrease of propene peaks or from the increase of the propane CH_3 signal amplitude in the spectrum detected using normal hydrogen (Supporting Information). At this temperature, the yield was quite low (ca. 6%). The PHIP enhancement, in turn, was determined by comparing the HP propane signal with the corresponding signal in the experiment performed with normal hydrogen. The enhancement was significant (ca. 60), thus emphasizing the crucial role of PHIP in the subsequent RD experiments. The signal-to-noise (SNR) ratio achieved in the PHIP experiment was about 10 per scan.

A spectacular demonstration of the enhancement provided by PHIP is shown in Figure 1d and e, where one-dimensional RD TOF images (see pulse sequence in the Supporting Information) obtained for the R-800-5 reactor using normal hydrogen and parahydrogen are compared. The SNR is superior in the latter case. The spatial encoding was performed along the reactor axis (*z* coordinate; Figure 1a), and the signal of propane produced in the reactor was utilized in the reconstruction of the images. These *z*-encoded RD experiments reveal the travel time of propane gas from different *z* locations in the reactor and outlet tubing to the detector, and therefore, the images quantitatively describe mass transport in the microfluidic system. The slope of the amplitude pattern reflects the flow velocities in different regions of the system; the larger slope corresponds to the higher flow velocity. The slopes were determined by linear fits to the *z* and *t* coordinates of maximum signal amplitudes. The flow velocity in the catalyst bed ($z > 23$ mm) was 0.35 cm s^{-1}, while it was 17 cm s^{-1} in the outlet capillary ($z < 23$ mm). The encoding coil $\pi/2$ pulse was about 820 times longer than that of the detection coil, implying that, according to the principle of reciprocity,[9] the sensitivity of the detection microcoil was 820 times better than that of the encoding coil. Therefore, the signal enhancement given by RD technique was about 820 with respect to a corresponding fictitious direct MRI experi-

 © 2012 Wiley-VCH Verlag GmbH & Co. KGaA, Weinheim

ment in which both signal encoding and detection are performed by the encoding coil. The overall sensitivity enhancement factor given by RD and PHIP was $820 \times 60 \approx 5 \times 10^4$. The signal amplitude in the transition region from the catalyst bed to the outlet capillary is almost zero. This may be a consequence of turbulence which distorts the phase encoding in that region. The turbulence may also increase the overall dispersion of the molecules encoded above the transition region. However, the overall dispersion is not very large, as can be seen in all the TOF images presented herein.

Apart from characterizing mass transport, we used z-encoded RD TOF experiments for in situ monitoring of the reaction product formation. The sum of the signals measured at different time instances (time projection) is directly proportional to the amount of propane, assuming that the catalyst packing is uniform and the effect of spin-lattice relaxation is insignificant.

When the final maximum amplitude of the time projection is normalized to correspond to the final reaction yield, which is determined in an independent experiment as described above, the time projection shows a quantitative estimate of the yield distribution in the catalyst bed.

The z-encoded TOF images acquired for R-800-5, R-405-14, and R-150-15 reactors at the elevated temperature (60 °C) are shown in Figure 2, along with the normalized time projections corresponding to the reaction yield distributions. Note that the final yield in R-800-5 reactor at this temperature is much higher (50 %) than at room temperature (6 %). On the other hand, the final yield in the R-150-15 reactor was much smaller (7 %) than in the other two reactors, which is most likely because of the shorter travel time of gas through the reactor.

To analyze the measured reaction yield curves, we derived a theoretical equation for the reaction yield X based on the plug-flow reactor (PFR) model and on the assumption that the order of the reaction between propene and hydrogen over silica-supported rhodium is approximately unity and zero with respect to hydrogen and propylene, respectively (see the Supporting Information). Furthermore, the equation takes the initial hydrogen/propene ratio in the experiments (2:1) into account. The model predicts that, if the inlet of the reactor is at $z = 0$, and z increases toward the outlet, then:

$$X(z) = 2\left[1 - e^{-\frac{kz}{u}}\right] \quad (1)$$

This continues until X reaches unity (k is the rate constant of the reaction and u is the flow velocity). Figure 2 shows that the model accounts for the experimental observations reasonably well. The quality of the fits tends to be better for smaller reactor size and lower reaction yields. It is possible that the gas flow in the largest reactor was not perfectly plug-like, because diffusional mixing is less efficient in a large reactor, and consequently PFR model does not work as accurately as in the smaller reactors. Another conceivable explanation could be that the reaction kinetics changes to some extent during the reaction process as the partial pressures of the reagents become lower.[13] Furthermore, temperature variations inside the larger reactors can be more significant, which also might influence the fitting quality. The effect of nuclear spin relaxation[14] (ignored above) is analyzed in detail in Supporting Information, and the analysis indicates that the relaxation influence is insignificant.

Gas flow in the reactors can be visualized in more detail by an RD MRI experiment with the spatial encoding performed in two orthogonal directions instead of only one (see pulse sequence in the Supporting Information). Such images measured for R-800-5, R-405-14, and R-150-15 reactors are shown in Figure 3 (see also the movies in the Supporting Information). Different panels correspond to the images observed at different travel time instants. The leftmost images are time projections; that is, the sums of all other panels. The SNR in the images is high, demonstrating that the sensitivity boost given by RD technique and PHIP is high enough for observing high quality TOF images even in the case when the signal is spread over two spatial dimensions.

The time projections highlight the signal in the reactor region in the case of the two larger reactors, because the cross-section of these reactors is much larger than that of the outlet tubing. However, even in these cases, the outlet tubing signal is visible in some individual panels, for example, in the $t =$ 86 ms panel in Figure 3a and in the $t = 62$ ms panel in Figure 3b. The images show that the two largest reactors are tilted because of their imperfect mounting inside the encoding coil. However, the tilting angle is exaggerated in the images because the horizontal (y) scale is significantly expanded as compared to the vertical (z) one. In reality, the angle is very small.

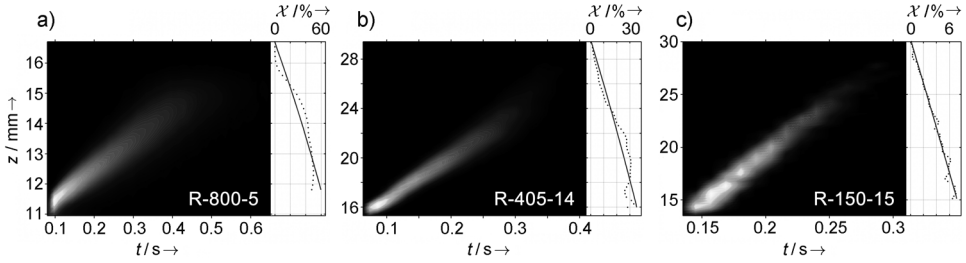

Figure 2. a)–c) z-Encoded RD TOF images measured for the Rh/SiO_2 catalyst bed in a) R-800-5, b) R-405-14, and c) R-150-15 reactors at 60 °C. The profiles on the right side of each image show the reaction yield variation along the catalyst bed axis. The dots and line correspond to the experimentally measured values and the best fits of the theoretical model function [Eq. (1)], respectively. The images were zoomed in to include only the catalyst bed regions, and acquired in 7 min with a time resolution of 12 ms and a spatial resolution of 310 (a), 540 (b), and 470 μm (c).

The signal in the panels measured at $t = 145$ and 204 ms in Figure 3a has a slightly parabolic shape, confirming that gas flow in the largest reactor is not perfectly plug-like, as was speculated above in the context of the PFR model. The length of the signal patch in the z direction increases with increasing travel time. The increase is larger in the case of the largest

 © 2012 Wiley-VCH Verlag GmbH & Co. KGaA, Weinheim

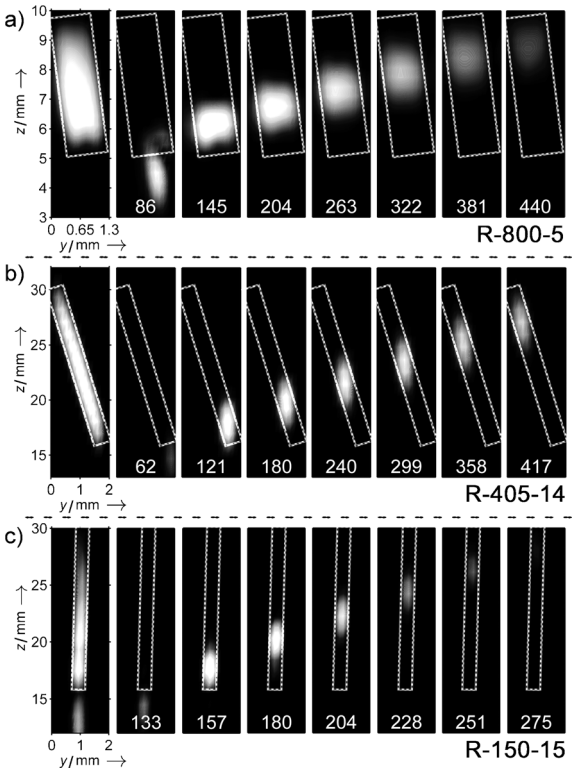

Figure 3. a)–c) *yz*-Encoded RD TOF images measured for Rh/SiO_2 catalyst beds in a) R-800-5, b) R-405-14, and c) R-150-15 reactors at 60 °C. The leftmost images are the time projections. Travel time instants in milliseconds are indicated in the panels. The catalyst bed regions are outlined with white dashed lines. The complete data set for each reactor was acquired in 13 min with a time resolution of 12 ms and a spatial resolution of 160–250 μm in the *y* direction and 0.62–2.2 mm in the *z* direction (see the Supporting Information).

reactor as compared to other reactors, meaning that the dispersion of gas molecules is highest in the largest reactor. This is most likely another implication of the non-plug-like flow. The signal in the time projection of the smallest reactor (Figure 3c) is patchy, and signal spots in the other panels are not perfectly symmetrical, which most likely reflects the inhomogeneities in the catalyst packing. The inhomogeneity is to be expected, because the particle size of the catalyst powder is comparable with the ID of the capillary in the case of the smallest reactor.

We found that the RD TOF experiments provide also detailed information about the adsorption–desorption processes taking place in the catalyst bed. The *z*-encoded TOF images shown in Figure 4 give an illustrative demonstration of this issue. The image in Figure 4a was measured for R-150-15 reactor, while the image in Figure 4b was measured for a similar reactor in which Rh/SiO_2 catalyst was replaced by Rh/TiO_2. In both cases, the ID of the reactor and the outlet tubing are equal. If the catalyst were an inert material that simply made the void space inside the reactor smaller, the gas-flow velocity in the reactor region would be larger than in the outlet tubing owing to the mass balance. However, the slopes in the TOF images show that the flow velocity in the reactor region is actually significantly smaller than in the outlet tubing. In Figure 4a, the velocity in the catalyst region was

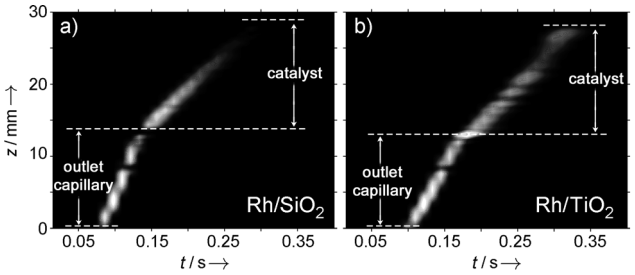

Figure 4. a), b) *z*-Encoded RD TOF images measured for a) Rh/SiO_2 and b) Rh/TiO_2 catalyst beds packed in the R-150-15 reactor. The catalyst bed and the outlet capillary regions are shown with white dashed lines in the images.

determined to be $u_{cat} = 8.8\ cm\,s^{-1}$, whereas the velocity in the outlet tubing was $u_{out} = 23.1\ cm\,s^{-1}$. The corresponding values in Figure 4b are $u_{cat} = 10.6\ cm\,s^{-1}$ and $u_{out} = 17.7\ cm\,s^{-1}$.

This apparent discrepancy is a consequence of gas adsorption; the bulk of the catalyst is a porous material (SiO_2 or TiO_2), which can adsorb gas molecules in significant quantities. Adsorption makes the average concentration of gas much higher in the catalyst region than in the outlet tubing, and consequently the average flow velocity in the catalyst region becomes lower than in the outlet tubing. Significant adsorption is manifested also in the image amplitudes; the integrated amplitude in the reactor region is much higher than in the outlet tubing. This is most clearly visualized in the *yz*-encoded images shown in Figure 3c.

We derived an equation predicting the relative velocities in the reactor and the outlet tubing (see the Supporting Information). The model is based on the mass balance consideration. The gas was assumed to be an ideal gas and the pressure drop in the flow system to be insignificant (experimentally verified by analyzing the change of the slope corresponding to the catalyst bed region; see the Supporting Information). Furthermore, we assumed that the flow and adsorption phenomena are independent processes; that is, each molecule undergoes a large number of adsorption–desorption events within the travel time. The resulting equation is:

$$\frac{u_{cat}}{u_{out}} = \frac{d_{out}^2}{d_{cat}^2}\left(\frac{1 + \nu_{pore}\rho_{solid}}{\phi + \nu_{pore}\rho_{solid} + (1-\phi)n_{ua}s\rho_{solid}\frac{RT}{P}}\right) \quad (2)$$

Equation (2) qualitatively predicts the observed reduction in the gas flow velocity in porous materials, and it implies that *z*-encoded RD TOF experiments can be used for a quantitative estimation of the amount of adsorbed gas if the properties of porous material are known. The description of symbols and the values of the essential parameters for SiO_2 used in this work are presented in the Supporting Information. By substituting these values and flow velocities determined from *z*-encoded TOF images into Equation (2), we calculated that the amount of adsorbed gas per unit area (n_{ua}) was 1.1×10^{-6}, 1.3×10^{-6}, and $2.7 \times 10^{-6}\ mol\,m^{-2}$ in R-800-5, R-405-14, and R-150-15 reactors, respectively. These values are larger than the known value n_{ua} for hydrogen,[15] but smaller than those for propane[16] and propene[16] adsorbed on SiO_2. This is

 © 2012 Wiley-VCH Verlag GmbH & Co. KGaA, Weinheim

reasonable, as we had the mixture of these three gases in the experiments, and thus the values confirm that the model works. However, the uncertainty of the calculated values is large, because instead of a single gas, a gas mixture was used, and inaccuracies in pressure P, temperature T, and porosity ϕ are large. In any case, the analysis helps us to understand the mass-transport phenomena in the reactors, and it shows that RD MRI provides an alternative means to measure adsorption isotherms in porous materials.

In summary, we have shown that microfluidic reactors can be used as miniaturized nuclear spin polarizers. Heterogeneous catalytic hydrogenation reaction resulted in a continuous flow of the catalyst-free hyperpolarized product. The sensitivity enhancement (about two orders of magnitude) given by these first reactor prototypes was already comparable with the enhancements provided by larger polarizers.[11a] The performance of the reactors was characterized by RD MRI. Altogether, the sensitivity boost given by RD MRI and PHIP was almost five orders of magnitude, allowing the power of NMR spectroscopy to be employed, despite the low filling factor and low concentration of molecules in the gas reactors. Apart from sensitivity improvement, RD MRI provided new capabilities for the studies of the microfluidic reactors. First, it enables unique information about mass transport phenomena in a microfluidic reactor to be extracted, such as flow paths, velocities and dispersion. Second, it also allows the spatial dependence of the reaction yield in the reactors to be measured, and consequently it provided information about reaction kinetics. Third, it provides a quantitative estimate of gas adsorption in the porous catalyst material. Consequently, RD MRI broadens significantly the limits of NMR for characterization of chemical reactors.

Experimental Section

Continuous-flow microfluidic reactors were made by connecting the cylindrical inlet capillary (ID 800, 405, or 150 μm) to the outlet capillary (ID 150 μm) inside the encoding coil (Figure 1 a). Solid catalyst powder was packed inside the inlet capillary close to the connection, and the length of the catalyst bed varied between 5 and 15 mm. Almost all of the experiments were performed using [Rh(cod)(sulfos)]/SiO_2 as the hydrogenation catalyst precursor (referred to as Rh/SiO_2 in the discussion); Rh/TiO_2 was used in some selected experiments for comparison. The reagent gas mixture contained propene, parahydrogen, and orthohydrogen in a circa 1:1:1 ratio. RD MRI experiments were performed on a Bruker DSX 300 spectrometer operating at 300 MHz proton resonance frequency. Spatial encoding was carried out by a Bruker Micro 2.5 imaging probe, using an RF insert with inner diameter and height of 25 and 35 mm, respectively. The detection coil was of 3 mm in length and made of 120 μm copper wire wound around a 360 μm Upchurch fused silica capillary (outlet capillary). The RD MRI pulse sequences used herein as well as other essential experimental details and procedures are described in the Supporting Information.

Received: April 18, 2012
Revised: May 18, 2012
Published online: July 2, 2012

Keywords: heterogeneous catalysis · microreactors · NMR imaging · remote detection · sensitivity enhancement

[1] a) S. Stapf, S.-I. Han, *NMR Imaging in Chemical Engineering*, Wiley-VCH, Weinheim, **2006**, p. 620; b) A. A. Lysova, I. V. Koptyug, *Chem. Soc. Rev.* **2010**, *39*, 4585 – 4601; c) L. F. Gladden, M. D. Mantle, A. J. Sederman in *Advances in Chemical Engineering*, *Vol. 30* (Ed.: B. M. Guy), Academic Press, **2005**, pp. 63 – 135; d) L. F. Gladden, M. D. Mantle, A. J. Sederman, *Adv. Catal.* **2006**, *50*, 1 – 75.

[2] A. Viale, S. Aime, *Curr. Opin. Chem. Biol.* **2010**, *14*, 90 – 96.

[3] a) C. R. Bowers, D. P. Weitekamp, *J. Am. Chem. Soc.* **1987**, *109*, 5541 – 5542; b) C. R. Bowers in *Encyclopedia of Nuclear Magnetic Resonance*, *Vol. 9* (Eds.: D. M. Gant, R. K. Harris), Wiley, Chichester, **2002**, pp. 750 – 769; c) S. B. Duckett, S. A. Colebrooke in *Encyclopedia of Nuclear Magnetic Resonance*, *Vol. 9* (Eds.: D. M. Gant, R. K. Harris), Wiley, Chichester, **2002**, pp. 598 – 620.

[4] a) I. V. Koptyug, K. V. Kovtunov, S. R. Burt, M. S. Anwar, C. Hilty, S. I. Han, A. Pines, R. Z. Sagdeev, *J. Am. Chem. Soc.* **2007**, *129*, 5580 – 5586; b) K. V. Kovtunov, I. E. Beck, V. I. Bukhtiyarov, I. V. Koptyug, *Angew. Chem.* **2008**, *120*, 1514 – 1517; *Angew. Chem. Int. Ed.* **2008**, *47*, 1492 – 1495.

[5] a) K. V. Kovtunov, V. V. Zhivonitko, A. Corma, I. V. Koptyug, *J. Phys. Chem. Lett.* **2010**, *1*, 1705 – 1708; b) K. V. Kovtunov, V. V. Zhivonitko, L. Kiwi-Minsker, I. V. Koptyug, *Chem. Commun.* **2010**, *46*, 5764 – 5766; c) A. M. Balu, S. B. Duckett, R. Luque, *Dalton Trans.* **2009**, 5074 – 5076; d) Q. X. Gong, J. Klankermayer, B. Blumich, *Chem. Eur. J.* **2011**, *17*, 13795 – 13799; e) R. Sharma, L. S. Bouchard, *Sci. Rep.* **2012**, *2*, 277.

[6] a) G. M. Whitesides, *Nature* **2006**, *442*, 368 – 373; b) G. S. Jeong, S. Chung, C. B. Kim, S. H. Lee, *Analyst* **2010**, *135*, 460 – 473; c) Y. K. Suh, S. Kang, *Micromachines* **2010**, *1*, 82 – 111; d) R. R. Pompano, W. Liu, W. Du, R. F. Ismagilov, *Annu. Rev. Anal. Chem.* **2011**, *4*, 59 – 81; e) K. Choi, A. H. C. Ng, R. Fobel, A. R. Wheeler, *Annu. Rev. Anal. Chem.* **2012**, *5*, 413 – 440.

[7] G. Centi, S. Perathoner in *Sustainable industrial processes* (Eds.: F. Cavani, G. Centi, S. Perathoner, F. Trifirò), Wiley-VCH, Weinheim, **2009**, pp. 199 – 256.

[8] K. F. Jensen, *Chem. Eng. Sci.* **2001**, *56*, 293 – 303.

[9] D. I. Hoult, R. E. Richards, *J. Magn. Reson.* **1976**, *24*, 71 – 85.

[10] a) A. J. Moule, M. M. Spence, S. I. Han, J. A. Seeley, K. L. Pierce, S. Saxena, A. Pines, *Proc. Natl. Acad. Sci. USA* **2003**, *100*, 9122 – 9127; b) J. A. Seeley, S. I. Han, A. Pines, *J. Magn. Reson.* **2004**, *167*, 282 – 290; c) J. Granwehr, E. Harel, S. Han, S. Garcia, A. Pines, P. N. Sen, Y. Q. Song, *Phys. Rev. Lett.* **2005**, *95*, 075503; d) E. E. McDonnell, S. I. Han, C. Hilty, K. L. Pierce, A. Pines, *Anal. Chem.* **2005**, *77*, 8109 – 8114; e) C. Hilty, E. E. McDonnell, J. Granwehr, K. L. Pierce, S. I. Han, A. Pines, *Proc. Natl. Acad. Sci. USA* **2005**, *102*, 14960 – 14963.

[11] a) V. V. Telkki, V. V. Zhivonitko, S. Ahola, K. V. Kovtunov, J. Jokisaari, I. V. Koptyug, *Angew. Chem.* **2010**, *122*, 8541 – 8544; *Angew. Chem. Int. Ed.* **2010**, *49*, 8363 – 8366; b) V.-V. Telkki, V. V. Zhivonitko, *J. Magn. Reson.* **2011**, *210*, 238 – 245.

[12] L. S. Bouchard, S. R. Burt, M. S. Anwar, K. V. Kovtunov, I. V. Koptyug, A. Pines, *Science* **2008**, *319*, 442 – 445.

[13] G. Webb in *Comprehensive Chemical Kinetics*, *Vol. 20* (Eds.: C. H. Bamford, C. F. H. Tipper), Elsevier, Dordrecht, **1978**, pp. 1 – 121.

[14] J. Granwehr, J. A. Seeley, *J. Magn. Reson.* **2006**, *179*, 280 – 289.

[15] M. van der Waarden, F. E. C. Scheffer, *Recl. Trav. Chim. Pays-Bas* **1952**, *71*, 689 – 698.

[16] W. K. Lewis, E. R. Gilliland, B. Chertow, W. H. Hoffman, *J. Am. Chem. Soc.* **1950**, *72*, 1153 – 1157.

 © 2012 Wiley-VCH Verlag GmbH & Co. KGaA, Weinheim